AIAA JOURNAL
Vol. 47, No. 10, October 2009

Shock-Train Structure Resolved with Absorption Spectroscopy Part 1: System Design and Validation

Chadwick D. Lindstrom,* Kevin R. Jackson,† and Skip Williams‡
U.S. Air Force Research Laboratory, Wright-Patterson Air Force Base, Ohio 45433
Ryan Givens§ and William F. Bailey¶
Air Force Institute of Technology, Wright-Patterson Air Force Base, Ohio 45433
Chung-Jen Tam**
Taitech, Inc., Beavercreek, Ohio 45430
and
William F. Terry††
Innovative Scientific Solutions, Inc., Beavercreek, Ohio 45430

DOI: 10.2514/1.41074

A multiple-line-of-sight tunable diode laser absorption system for measuring shock-train structure inside a model scramjet isolator at the Wright-Patterson Air Force Base Propulsion Directorate's research cell 18 supersonic combustion facility is described. Multiple rovibrational lines of water are probed using time-multiplexing of multiple diode lasers projected across a rectangular isolator duct along 16 lines of sight. Static temperatures and water concentration (path-averaged) are computed from a Boltzmann plot for the multiple lines that are measured, and static pressures are determined from the absorption line width. The experimental setup and measurement technique are presented here along with the Mach 2 flow (no shock train) results. The absorption measurements agree to within 2% of sidewall pressure transducer measurements and calculated (path-averaged) static temperatures at 5 Hz. The motivation for the development of this sensor was to demonstrate that it is possible to obtain accurate tunable diode laser absorption spectroscopy measurements over multiple lines of sight in a supersonic flow in real-time, allowing useful data about the spatial and temporal changes of the static pressure and temperature within a supersonic shock train. The present measurements demonstrate that multiple-line-of-sight measurements can obtain temperature, pressure, and water density information with an overall accuracy better than 5% at 1000 Hz and show that sensing based on real-time tunable diode laser absorption spectroscopy of supersonic flows is possible.

Nomenclature

A	=	frequency-integrated absorbance
A_ν	=	absorbance at frequency ν
E''	=	lower-state energy
g	=	line-shape function
I	=	transmitted laser intensity
I_0	=	initial laser intensity
J	=	total angular momentum
J', K'_a, K'_c	=	upper-state rotational labels
J'', K''_a, K''_c	=	lower-state rotational labels
Ka, Kc	=	asymmetric tops
L	=	path length
N_T, N_{H_2O}	=	total density of the absorbing species (H_2O specifically)
n	=	temperature coefficient for collisional broadening coefficients
S	=	line intensity (reference is at 296 K)
$\tilde{\alpha}$	=	frequency-integrated absorption coefficient
α_ν	=	absorption coefficient at frequency ν
γ_D	=	Doppler broadening coefficient
γ_L	=	collisional broadening coefficient
ΔN	=	difference in quantum-state density, taking into account degeneracy factors
ν	=	frequency
ν_{10}	=	peak transition frequency for an absorption line
ν'_1, ν'_2, ν'_3	=	upper-state vibrational quantum numbers for symmetric stretch, bend, and asymmetric stretch
σ_ν	=	absorption cross section at frequency ν
χ	=	mole fraction

Received 17 September 2008; revision received 12 May 2009; accepted for publication 26 May 2009.

*National Research Council Postdoctoral Fellow, Propulsion Directorate, Aerospace Propulsion Division. Member AIAA.
†Research Engineer, Propulsion Directorate, Aerospace Propulsion Division. Member AIAA.
‡Principal Research Physicist, Propulsion Directorate, Aerospace Propulsion Division. Senior Member AIAA.
§M.S. Student, Department of Engineering Physics.
¶Professor, Department of Engineering Physics. Member AIAA.
**Senior Research Scientist. Associate Fellow AIAA.
††Senior Technician. Member AIAA.

I. Introduction

TUNABLE diode laser absorption spectroscopy (TDLAS) is a relatively mature technique for making in-laboratory measurements of gas species concentrations such as water (H_2O) (the focus of the current study) and static temperature in homogenous environments [1–3]. However, application of this technique for monitoring high-speed flows such as afterburner exhaust plumes of jet engines, supersonic combustors, and gas turbines is under development. Here, the dynamic and spatially inhomogeneous nature of the flows makes application of this line-of-sight (LOS) technique difficult. For example, the supersonic flow introduces scintillation effects due to high-speed turbulence, as discussed in one of our previous works [4]. Spatial inhomogeneities must be addressed as well. Ideally, it is necessary to probe multiple spatial locations simultaneously at a rapid measurement rate to develop an understanding of the flowfield. Most previous attempts to make measurements in supersonic flows have focused to a large extent either on one or two path-averaged measurements or the use of a single line of sight scanned across the flow [4–6]. Although these approaches yield valuable information about uniform flows, they will fail when confronted with dynamic

flows that change both in time and space. This current effort shows that it is possible to obtain significant information about dynamic spatially and temporally changing flows using TDLAS with multiple LOS. In addition, it is found that the use of multiple LOS can improve the overall data quality for supersonic flows with no-shock structures. Ultimately, it is hoped that this effort will help pave the way for more sophisticated tomographic techniques to be applied to supersonic flows.

In this two-part series, the observation of the static pressure, temperature, and density fluctuations in a supersonic shock train of a model scramjet isolator is explored using a TDLAS sensor based on 16 LOS. This particular problem has been chosen for several reasons. Significant interest exists in the development of air mass-flux or mass-flow sensors for in-flight measurements based on TDLAS technology for aerospace applications [4,7–9]. Although excellent measurement accuracy to the level of 1% has been previously reported for low-speed flows [8], the conditions found in scramjet isolators pose significant new challenges. Based on the engine operating conditions in addition to the problems of boundary-layer effects, the flow is typically turbulent because of high Reynolds numbers and shock structures that can be present. By combining 14 LOS with 2 diagonal LOS for velocity measurements, it is possible to begin to develop an understanding of the influence that shock trains have on mass-flux measurements, although this will not be the current focus of the two-part series. Instead, the interest of this research is on the structure of the shock train itself. Much is known about supersonic shock trains in ducts that result from the interaction of shocks with the boundary layer [10]. In a supersonic shock train, a sequence of shocks forms in the streamwise direction that depends to a large extent on the Mach number and boundary-layer thickness. Although the flow is truly three-dimensional in nature, the dominant variations occur in the streamwise direction, and so significant information about the shock-train structure can be obtained by probing that direction of the flow. This symmetry simplified the experimental setup considerably and allowed tests to be conducted with existing optical access hardware probing only in the streamwise direction. In the future, it should be possible to extend these measurements by probing the transverse direction as well, at the cost of a more complex setup. Much information has been obtained using wall measurements of this phenomena, but it is limited to determining the shock-front location, and much less information exists about shock-train inflow properties as well as dynamics [10]. Here, the goal is to obtain time-dependent inflow data (1 kHz) at several spatial locations along the flow direction that can be compared with theory as well as computational fluid dynamics (CFD) simulations. Traditionally, these flow properties have been explored using particle velocimetry techniques, high-speed schlieren, and in-stream pressure probes [11–13]. Studies using these techniques focused on slower flows ($M \approx 1.6$) than those studied here ($M \approx 2.2$), for which the shock-train unsteadiness was less and the shock train was known to be a normal shock train. The use of TDLAS can complement these measurements while offering the significant advantage of miniaturization, thus allowing the possibility of in-flight measurements in addition to ground testing.

In the current paper, the system design, measurement technique, and Mach 2 flow results will be presented. This allows comparison of system performance with previous measurements [5,6,14,15] that have been made in the literature as well as with conventional pressure transducer and thermocouple measurements. Also introduced here is the use of collisional broadening to measure the static pressure in a supersonic flow. Although collisional broadening has been well known since the beginning of spectroscopic techniques [16], to our knowledge it has not been exploited in the measurement of supersonic flows. Probably the most significant reason for this is that previous campaigns have not been interested in flows with substantial pressure variations. However, there is also the issue of accurately knowing the line-broadening parameters, which are continually improving with the increased accuracy of both measurements and calculations [17–20]. Here, it will be shown that accurate measurements of pressure can be made if the line parameters are well known.

II. Measurement Technique

This section starts with an overview of the notation used in this paper and the next. Because of the ubiquity of the use of absorption spectroscopy in multiple fields, many different notations are used to describe the same phenomenon [21–23]. For clarification, the particular formulation used here is subsequently described briefly and follows that defined in the HITRAN database [20,24]. Next, the particular absorption lines for H_2O used in this study are described as well as their spectroscopic line parameters. This is followed by a brief discussion of how the static temperature is determined from the multiple absorption features. Finally, a description of how the static pressure is determined from line width is given. As mentioned in the Introduction, this represents one of the first attempts to make this type of measurement in supersonic flow and so a simulation that assesses the impact of the boundary layer on the accuracy of the measurement is presented. This section also addresses the accuracy of available pressure-broadening coefficients that are available from literature and the impact on the static pressure measurement.

Beer's law describes the attenuation of light as it passes through an absorbing medium [21]:

$$I = I_0 e^{-\sigma_\nu \Delta N L} = I_0 e^{-\alpha_\nu L} \rightarrow \ell_n\left(\frac{I_0}{I}\right) = A_\nu = \alpha_\nu L \tag{1}$$

where I is the transmitted laser intensity through the medium; I_0 is the initial intensity; σ_ν is the absorption cross section at the frequency ν; ΔN is the difference between upper- and lower-state quantum-state densities, taking into account degeneracy factors (total quantum-state fractional population times the total species density); L is the path length through the absorbing medium; and α_ν is the absorption coefficient at the frequency ν. The absorbance A_ν shown in Eq. (1) is plotted in this paper rather than the actual intensity. This is done by dividing through with a reference signal that is recorded in addition to the measurement paths. However, Eq. (1) is not in a convenient form for comparison with what is typically tabulated in spectroscopy databases such as HITRAN [20]. These databases replace the absorption cross section with the line intensity $S(T)$ and a line-shape function $g(\nu - \nu_{10})$ that describes the spectral line shape, where ν_{10} is the peak center. In addition, the line intensity also incorporates a Boltzmann factor that accounts for the thermal populations of the rovibrational states involved in the transition, which is the reason for the line shape's dependence on temperature. With these changes, Beer's law becomes

$$I = I_0 e^{-S(T) g(\nu - \nu_{10}) N_T L} \rightarrow A_\nu = S(T) g(\nu - \nu_{10}) N_T L \tag{2}$$

where N_T is the total density of the absorbing species. The line-shape function is normalized such that integration over frequency or wave number yields a value of unity. The data here can be described by a Voigt line-shape function, computed using the Humlíček algorithm [25], which takes into account the collisional broadening and the Doppler broadening through the convolution of a Gaussian with a Lorentzian [21]. This means that if Eq. (2) is integrated over frequency, then the frequency-integrated absorption is related to the line intensity and the column density $N_T L$ through the following relation:

$$\int_{-\infty}^{\infty} A_\nu \, \mathrm{d}\nu = A = S(T) N_T L = \tilde{\alpha} L \tag{3}$$

where the frequency-integrated absorbance A and the frequency-integrated absorption coefficient $\tilde{\alpha}$ have been introduced. The frequency-integrated absorption coefficient has been introduced because it makes description of inhomogeneous flowfields particularly simple. In that case, the frequency-integrated absorbance is given by

$$A = \int_{\text{path}} \tilde{\alpha}(l) \, \mathrm{d}l \tag{4}$$

This is an innocuous-looking formula that can actually be very difficult to compute, because with the adoption of the HITRAN line

strength in Eq. (3), $\tilde{\alpha}$ is a complicated function of temperature and pressure. For example, if significant variations in the line shape occur because of variations in absorbing species temperature, density, and total density, then computation of A will require more than a single Voigt line shape to fit the absorption peak [14,26]. Fit residuals showed that a single Voigt line shape is sufficient to examine the isolator data. Another obvious aspect is that if local flow information is desired, then it becomes necessary to use some form of tomographic inversion or flowfield model to help determine $\tilde{\alpha}$ [14,15,27–30]. For the isolator experiments, CFD simulations are used to compute the frequency-integrated absorption that can then be used to compare the simulations with the measurements. This is done in two steps:

1) An image or map of the frequency-integrated absorption coefficient is generated from the temperature and densities computed by CFD.

2) The path integration is done numerically using a trapezoidal integration routine.

The frequency-integrated absorption for each absorption feature can then be input into the routine to compute the temperature and species concentration from a Boltzmann plot. This allows direct comparisons between the CFD and path-integrated measurements to be made.

A. Spectral Line Parameters and Sample Spectra

Water vapor has several strong rovibrational spectroscopic transitions from the visible to the midinfrared. The availability of compact spectroscopic quality lasers at telecom wavelengths (1250–1650 nm) have made the $2\nu_1$, $2\nu_3$, and $\nu_{1+}\nu_3$ vibrational bands particularly attractive for diagnostic applications. The abundance of water vapor as a primary combustion product and the relatively large line strengths for these transitions enable these transitions to be used with good sensitivity for many applications.

Single-mode fiber-coupled distributed feedback lasers are used to generate near-infrared radiation to measure H_2O line intensities in the spectral regions 7184.2–7186.4 cm^{-1}, 7159.5–7161.5 cm^{-1}, and 7179.5–7181.8 cm^{-1}. Principally, P and Q branch transitions of the $\nu_1 + \nu_3$ band have been used in this study, as identified by the lowercase letters in Fig. 1. The isolator was not backpressured during the time when the data were taken. As can be seen in the figure, peaks a–d are quite strong, thus they are used to determine the temperature and water concentration in the isolator. Peak a is also used to determine the static pressure in the isolator. A small side peak c′ (shown in Table 1) is close to feature c, but feature c is a much stronger transition. In addition, peak c′ shares the same initial state with peak d, and so its area can easily be subtracted from the peak integration. Finally, e–f have much higher initial state energies and so are only used for much higher temperatures. The data quality of the time-averaged data is excellent as shown in Fig. 1, with the residuals being less than 1% of the maximum peak amplitude when using a multipeak Voigt algorithm. Here, the reference beam measurement is initially divided by the raw data after both have been appropriately scaled to match in the regions outside of the absorption peaks. Then a cubic polynomial and Voigt peaks are fitted to the natural logarithm of the resulting spectrum. The cubic polynomial corrects for any nonlinearity that is present as the laser rapidly scans across the spectral region.

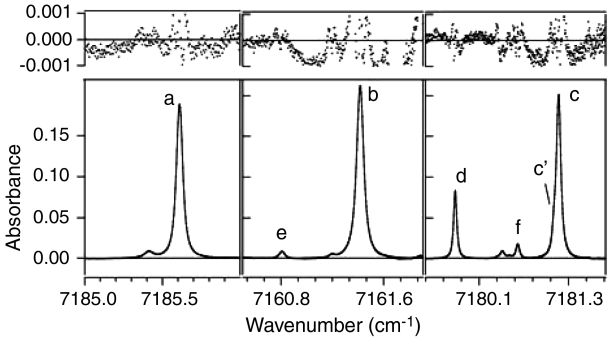

Fig. 1 Time-averaged (200 averages) spectra, fit, and residuals for the three spectral regions during run AC (see Table 3).

The line parameters listed in Table 1 are taken from the HITRAN 2004 database. The line intensities at different temperatures are derived using the same procedures and partition function expressions as defined in HITRAN [20]. Here, the line parameters have been taken from the HITRAN 2004 database because it is the most complete source and it compares well with recent studies [18,19]. Some of these transitions have been studied by several authors, and the variation among them is between 2–5%, depending on the parameter [18–20,31,32]. In this study, the HITRAN parameters are used which means systematic errors less than 5% [19] may be present in the following analysis based on these line parameters. It is possible to reduce the systematic error through careful self-calibration of the system over the temperature and pressure range of interest, however, this was not done here because it requires a special setup.

B. Determination of Temperature from a Boltzmann Plot

The determination of path-averaged static temperature is accomplished by measuring multiple absorption features of the same molecule. The frequency-integrated absorption is normalized by the cross section and degeneracy factor for each transition and then plotted versus the initial state energy divided by k_B. In terms of the preceding line intensity, this results in the following relationship:

$$\ell_n\left(\frac{A}{S_{\text{ref}}}e^{-E''/k_BT_{\text{ref}}}(1-e^{-h\nu_{10}/k_BT_{\text{ref}}})\right) = -\frac{E''}{k_BT} + \ell_n\left(\frac{Q(T_{\text{ref}})}{Q(T)}N_TL\right) + \ell_n(1-e^{-h\nu_{10}/k_BT}) \tag{5}$$

where $Q(T)$ is the partition function for the absorbing species and E'' is the initial state energy. At the temperatures and transition frequencies studied here, the stimulated emission terms can be ignored (i.e., $e^{-h\nu_{10}/KT} \approx 0$). Figure 2 shows a typical Boltzmann plot for the Mach 2 flow (no shock) taken during run condition AC. Here, four water transitions are used to compute the path-integrated temperature. The curve shows excellent linearity which is indicative of a nearly uniform temperature distribution. The slope of the curve is inversely proportional to temperature and can be directly determined from the linear fit. In contrast, the partition function [20] must be used to determine the species concentration either from the slope of the curve or through using the measured temperature and the frequency-integrated absorption of one of the transitions.

Table 1 Spectroscopic line parameters

λ, nm	ν_{10}, cm^{-1}	S at 296 K, cm^{-1}/molecule-cm^{-2}	E'', cm^{-1}	ν_1', ν_2', ν_3'	J', K_a', K_c'	J'', K_a'', K_c''	Label
1391.67	7185.60	7.947e − 22	1045.06	1, 0, 1	6, 6, 0	6, 6, 1	a
1396.37	7161.41	1.174e − 20	224.84	1, 0, 1	3, 1, 3	4, 1, 4	b
1392.53	7181.16	1.505e − 20	136.76	1, 0, 1	2, 0, 2	3, 0, 3	c
1392.81	7179.75	2.299e − 22	1216.19	1, 0, 1	7, 6, 2	7, 6, 1	d
1396.49	7160.81	5.406e − 24	1874.97	1, 0, 1	10, 6, 4	10, 6, 5	e
1392.64	7180.61	3.038e − 23	1477.30	1, 0, 1	9, 5, 5	9, 5, 4	f
1392.55	7181.10	6.858e − 23	1216.19	1, 2, 0	7, 7, 0	7, 6, 1	c′

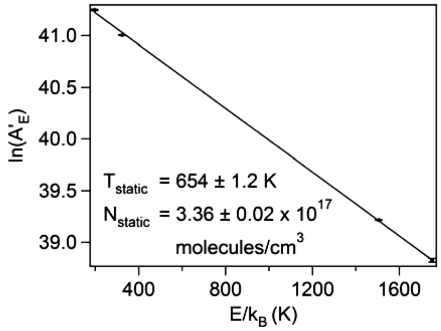

Fig. 2 Boltzmann plot for run AC using the LOS average data from a single beam path. The error bars are standard errors derived from the curve-fitting procedure and do not include errors associated with spatial variations in the flow as well as the effect of systematic errors in the line-shape parameters.

C. Determination of Static Pressure from Line Width

Static pressure can be determined from the collisional broadening of the absorption line. The width of the peak is proportional to two factors. The first factor is Doppler broadening, which is due to the thermal distribution of the velocity of the molecules in the gas. This is independent of the states involved in the transition and takes the form of a Gaussian line shape with a half-width at half-maximum of

$$\gamma_D = 3.5812 \times 10^{-7} \nu_0 \sqrt{\frac{T}{M}} \tag{6}$$

where the transition frequency ν_0 is given in wave numbers, T is the gas temperature in K, and M is the molecular mass in grams/mole. At the temperatures in the isolator (400–650 K), γ_D ranges from 0.012–0.015 cm^{-1} for lines such as the 7185.6 cm^{-1} feature, and thus the Doppler broadening is of the same magnitude as the collisional broadening. It is therefore desirable to first estimate the temperature using the Boltzmann plot to fix γ_D. This allows the determination of the collisional broadening from the Voigt fit using the Lorentzian width.

An important consideration when determining pressure in the manner described earlier is the approximation of the absorption line by a single Voigt peak. In reality, in the case of Mach 2 duct flow (no shock), the temperature and density change near the sidewall due to the boundary layer, with only slight pressure variations (on the order of 1%). In the presence of a shock structure such as that described in the companion paper, it is necessary to validate the appropriateness of using a single Voigt profile with significant pressure, temperature, and density inhomogeneities along the LOS. In severe cases, the line shape should be represented as a superposition of Voigt profiles. To assess the effect of the approximation, simulations have been conducted using the results of CFD, both here for the no-shock case and in part 2 of this paper for the case of a shock (part 2 addresses how the CFD flow simulations were calculated). In Fig. 3, the upper plot shows a pseudo color plot of the temperature for a vertical cross section of the isolator duct. As can be seen, there is a temperature gradient of approximately 200 K through the boundary layer. Because of this temperature gradient, the path-integrated temperature is higher (630 K) than the temperature at the centerline of the duct, which is 613 K. Despite the temperature gradient and the subsequent density gradient (pressure gradients are small here: ~1%), the single line Voigt does an excellent job fitting the composite line shape, as indicated by the residuals in this figure. The oscillation in the residuals plot is the result of trying to fit a composite line shape with a single Voigt, as described elsewhere [14,26]. Perhaps the most significant aspect of the plot is the excellent agreement between the static pressure determined from the fit and the static pressure at the duct centerline. This shows that the boundary-layer effects on the current static pressure measurements should be minimal for the Mach 2 flow analyzed in this paper.

Collisional broadening is dependent on the gas molecules involved in the collisions as well as their quantum states. This

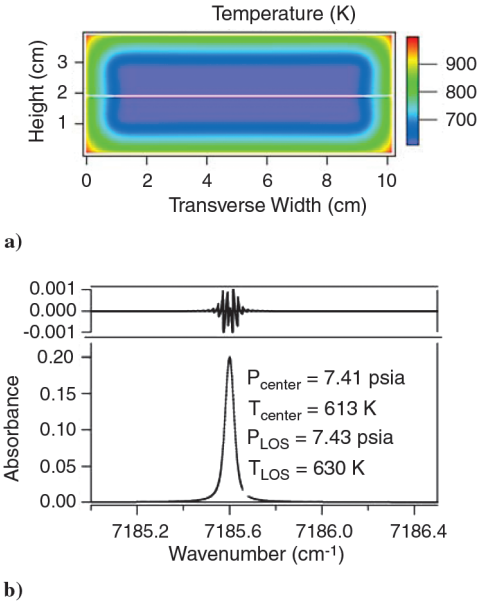

Fig. 3 Plots of a) 2-D CFD temperature profile in the isolator (flow direction is out of the page) for run condition AC as the LOS that is being used to calculate the path-averaged measurement and b) CFD simulated line shape, curve-fitted to a single Voigt profile and residuals, and the LOS pressure and temperature from the fit compared with the pressure and temperature at the centerline of the isolator.

dependence necessitates the use of different Lorentzian broadening parameters for each transition, and these parameters must be determined for each type of collision partner over the relevant range of conditions for the gas mixture being probed. A molar-based addition of the broadening coefficients for a given temperature yields the total collisional broadening coefficient γ_L. For the vitiated gas mixture present in the isolator, the collisional broadening coefficient γ_L is defined in Eq. (7) as

$$\gamma_L = \chi_{H_2O}\gamma_{H_2O-H_2O}\left(\frac{T_{ref}}{T}\right)^{n_{H_2O}} + \chi_{N_2}\gamma_{N_2-H_2O}\left(\frac{T_{ref}}{T}\right)^{n_{N_2}} + \chi_{O_2}\gamma_{O_2-H_2O}\left(\frac{T_{ref}}{T}\right)^{n_{O_2}} + \chi_{CO_2}\gamma_{CO_2-H_2O}\left(\frac{T_{ref}}{T}\right)^{n_{CO_2}} \tag{7}$$

where χ is the mole fraction of the particular species and the species-specific broadening coefficients for the major flow constituents are used, T_{ref} is the reference temperature (296 K here), T is the gas temperature, and n is the temperature coefficient. The particular mole fraction of the major flow constituents is determined from calibrated mass flow and measured greater than 99.9% combustion efficiency of the vitiator. Because four broadening coefficients and temperature coefficients are required, it is difficult to find a single literature source that has a complete set. The computational work of Delaye et al. [17] lists the required quantities. However, as pointed out by Nagali et al. [33], the temperature coefficients can have significant error for the 7185.6 cm^{-1} line. The self-broadening coefficient of H_2O in the work of Nagali et al., however, disagrees with a more recent measurement of Lepere et al. [31]. In addition, neither experimental author reports a temperature coefficient for the oxygen line-broadening parameter. These disagreements are not uncommon and a critical, although somewhat dated, review of problems associated with collisional broadening parameters for water-vapor lines is given in the work of Gamache et al. [34]. As stated there, disagreements within line parameters can lead to variations in estimated pressure on the order of 10%. Here, the most current line-broadening parameters from the literature sources cited earlier and a recent study by Durry et al. [18] of N_2 and O_2 broadening are combined. The line parameters for the 7185.6 cm^{-1} line used in this study are listed in Table 2.

Table 2 Broadening parameters and temperature coefficients for line *a* (7185.6 cm^{-1})

Perturbing species	γ at 296 K, $cm^{-1} \cdot atm^{-1}$	Temperature coefficient n
H_2O	0.23[31]	0.56[33]
N_2	0.0456[18]	0.64[33]
O_2	0.0271[18]	0.49[17]
CO_2	0.086[33]	0.74[33]

III. Experimental Setup and Design

This section first describes the multiple-line-of-sight (MLOS) tunable diode laser absorption system that has been assembled from commercial components as well as in-house-designed electronics and hardware. Next, the test setup is described as well as the run conditions that are analyzed in Sec. IV.

A. MLOS Tunable Diode Laser Absorption System

The system that has been constructed for MLOS-TDLAS consists of two primary components. The first is the optical components that combine the time-multiplexed outputs of the diode lasers and then split the combined beam into 16 separate beams for projection across the flow. The second is the electronics that drive the lasers as well as the data acquisition system and photodiode arrays that collect and digitize the transmitted light. Here, the key components of each are described.

Figure 4 shows a schematic of the common optical components used in each experimental setup. Three distributed feedback diode lasers (NEL NLK1E5GAAA), all operating in different spectral regions, are time-multiplexed in a single period lasting 1 μs and combined using a 1×4 combiner (Newport F-CPL-B14350). The combined beam is then split using a 10/90 splitter (Newport F-CPL-B12351), with the 10% beam going to a 50/50 splitter (Newport F-CPL-B12355) for which the output is routed to either a SiO_2 (Los Gatos Research) etalon with a $2.000 + 0.002$ GHz at 1550 nm free spectral range that monitors the frequency spectrum of the lasers or to a photodetector (Thorlabs PDA 400) that is used as a reference. The remaining 90% of the beam enters another 50/50 splitter that then connects to two 1×8 fiber optic splitters (Newport F-CPL-1×8-OPT) that are then collimated (Thorlabs F240APC-C, 8 mm focal length). The signal is attenuated by a factor of -18.5 dB as it passes through the splitters, and each LOS will observe an average power of 280 μW if the average input power of the lasers is 20 mW. This power level allows an excellent signal-to-noise ratio with the detector arrays, as can be seen in Fig. 1. The collimators are mounted on a precision-drilled base plate to enable tight beam placement. Because of the physical limitations of the optical mounts, the spacing of the collimator arrays is slightly larger than the 3 in. photodiode array used for detection.

The raw transmitted laser power is measured simultaneously on all 16 paths through the use of in-house custom-designed InGaAs photodiode arrays. These custom-designed arrays amplify the signal from 2-mm-diam FGA21 photodiodes (FGA 21 from ThorLabs) using a Texas Instruments OPA380 transimpedance amplifier for each photodiode. This amplifier with 90 MHz of gain bandwidth is a single supply (+5 V) and therefore requires a bias be applied to the photodiode so that input voltages are not driving to 0 V. The simplified schematic of the optical amplifier circuit is shown in Fig. 5. Several design tradeoffs were made in the circuit design to allow for an easily scalable system as well as ease of use. A 256-tap, 200 kΩ digital potentiometer (AD5262) allows for the gain to be controlled digitally. The leads to an additional 25 pF of parasitic capacitance that decreases the bandwidth and, combined with the photodiode junction capacitance of 500 pF at 0 bias voltage (at 0.5 V bias it is less), yields a total input capacitance of 525 pF. This capacitance with gain setting of 30 kΩ results in an overall bandwidth of approximately 950 kHz, as determined from the manufacturer's data sheet. At 200 kΩ the bandwidth of the circuit will decrease to 370 kHz. Although this seems considerably faster than the 1 kHz scan rate, the primary issue is the scan time across the peak, which is approximately 5.6 μs here. The frequency response must be faster to get a correct peak shape and area, which is the case for the nominal 30 kΩ feedback resistor used here; however, at high gains this can become a problem. This can be improved by moving to faster amplifiers with a larger gain-bandwidth product. The use of smaller photodiodes are possible as well; however, noise due to optical turbulence increases as the photodiode area decreases if the beam overfills the detector [4]. Clearly, improvements can be made to these photodiode arrays; however, the signal is still excellent for the size of the measured absorption peaks in Fig. 1.

After amplification by the photodiode array, the signal is digitized into 14 bits using a National Instruments (NI) PXI-6133 (32 million samples of onboard memory) S-series multifunction digital acquisition (DAQ) device sampling at a rate of 2.5 million samples/second. The amplifier output as well as all control signals and power are provided through a 68-wire cable that connects directly to the photodiode array using a SCSI-3-type connector. This, along with adaptable software written in-house, allows for easy scalability of the system, because each digitizer card and photodiode array provide an additional eight channels. A PXI chassis is used to hold all of the data acquisition equipment (i.e., computer/controller, DAQ cards, and the function generators used to drive the lasers). Because of the unsteady nature of the shock, a NI Intel Core Duo

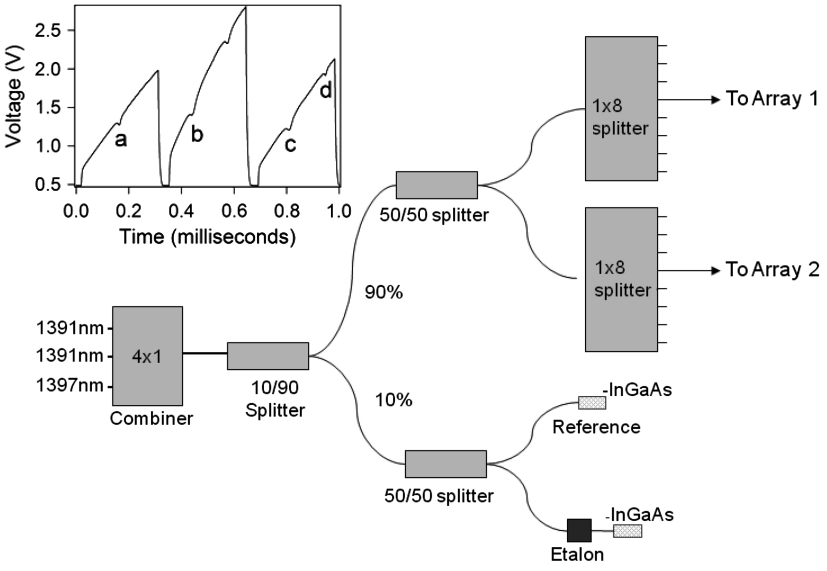

Fig. 4 Optical layout of multiplexed diode laser system and time-multiplexed signal (inset) with peaks labeled as indicated in Fig. 1 and Table 1.

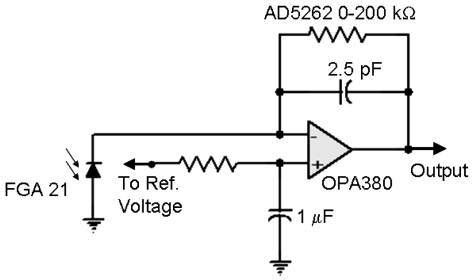

Fig. 5 Simplified schematic of the optical amplifier circuit.

2.0 GHz processor with 2 GB of DDR2 host RAM is used to average 200 spectra, determine peak areas through trapezoidal integration, and then create a real-time (1–5 Hz) LOS image along the flow direction. This provides feedback as to the success of the data runs. It also provides control of the current ramp of laser diodes through a NI PXI-5402 function generator. The digitizers and function generators are synchronized to approximately 5 ns using a 10 MHz backplane clock signal. Because all the channels are sampled simultaneously ($18 \times 2.5 \times 2 = 90$ MB/s), the bus in the PXI chassis cannot sustain continuous data transfer to the hard drive in the current configuration. Instead, a short segment of data (0.2 s) is captured, processed, and saved to the hard drive. This process takes approximately 5 s and then another 0.2 s of data are captured, processed, and saved. The data during the 0.2 s interval are taken continuously with 1 μs resolution and are only averaged later to improve the signal-to-noise ratio. This measurement process means that the frequency response of the instrument lies within two ranges: 1) less than 0.1 Hz (changes that occur between 5 s data segments and 2) 5 Hz (one 0.2 s period) to 500 Hz (Nyquist frequency). Although the shock is unsteady, pushing the shock slowly from the rear of the isolator to the front enables the key shock features to be measured. This enables shock-front oscillations up to several 100 Hz to be observed. The data acquisition/processing software was developed in LabWindows to allow a scalable architecture for developing TDLAS-based tomography.

B. Isolator Test Setup

This section first describes the direct connect supersonic combustion facility in which the experiment was performed and then describes the run conditions as well as the layout used for the actual test campaign. Figure 6 shows a schematic of the research cell 18, in which the experiments were performed. This facility was designed to allow basic studies of supersonic reacting flows using conventional and nonintrusive diagnostic techniques. It consists of a natural-gas-fueled vitiator, transition flange, interchangeable facility nozzle (Mach 1.8 and 2.2 are currently available), modular isolator, modular combustor, instrument section, and calorimeter. The test rig is provided with continuous flow of up to 30 lbm/s at 750 psia at a temperature of up to 922 K and exhausts into a 3.5 psia continuous-flow exhauster system. The facility can simulate flight conditions from Mach 3.5 to 5 at flight dynamic pressures of up to 2000 psf. For the current study, the combustor was removed and replaced with a large valve allowing simulation of the pressure rise associated with combustion. The isolator is fitted with 1-in.-high by 3.4-in.-wide optical access ports designed to hold 1.7-cm-thick (0.68-in.-thick) quartz windows or steel inserts. The quartz windows are wedged at 5 deg on the outer surface to prevent etaloning. The nozzle and isolator are instrumented with static pressure taps and thermocouple, with a frequency response of approximately 10 Hz. No difference in isolator performance has been noted between using the quartz windows or the thermal-barrier-coated (TBC) steel inserts, despite the differences in surface roughness between the quartz and the TBC. A key enabling aspect provided by this facility is that the vitiation that is used to increase the flow enthalpy to the correct level provides the water vapor being probed in this experiment. Although it is possible to measure oxygen, it is difficult to achieve the excellent signal-to-noise ratio that can be obtained with water-absorption features. More details can be found elsewhere [4,35,36].

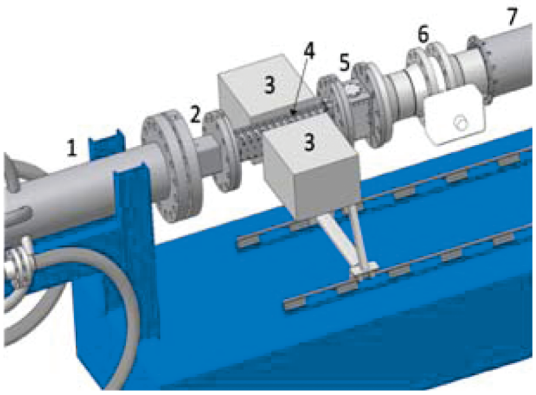

a)

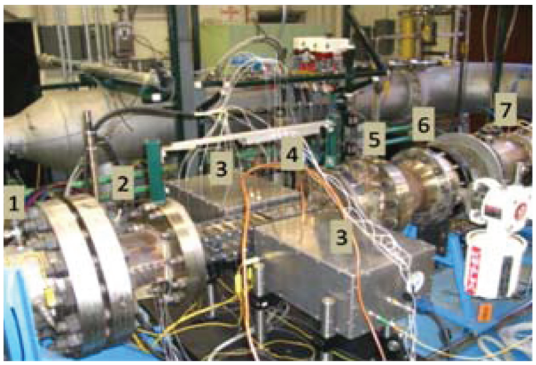

b)

Fig. 6 Supersonic combustion test facility: a) schematic and b) photograph indicating 1: vitiator, 2: facility nozzle, 3: TDLAS hardware, 4: isolator, 5: extension, 6: backpressure valve, and 7: exhaust line.

In the current paper, the analysis will focus on four sets of data labeled runs AB, AC, AF, and AG. These runs were chosen because of the different levels of water concentration and because the total temperature and pressure could be divided into two sets: (AB,AF) and (AC,AG). The vitiator settings as well as the nozzle Mach number, water molar percent, and Reynolds number for each case are shown in Table 3. The Reynolds number has been computed using the equivalent duct diameter (5.75 cm) for a rectangular duct with a cross section of 3.81×10.16 cm. The amount of vitiation used for each run depended on the desired total temperature and whether the air was preheated using electric heaters. The temperature and total pressure showed only a few degrees and about a 0.5 psia variation over the course of a data-collection cycle, meaning that they are accurate to 1% over the course of a test run. The water molar concentration, though, has to be computed from the mass flows of the compressed natural gas (CNG) and oxygen. In this case, several issues exist. First, CNG is not pure methane but includes CO_2 and larger alkanes such as ethane and propane. The presence of CO_2 will lower the amount of water in the vitiated flow, but the combustion of larger alkanes will increase it. The CNG used in these experiments is composed of 95.19% methane, 2.30% ethane, 1.28% CO_2, 0.65% nitrogen, and 0.58% higher alkanes (propane, butane, pentane, etc.) based on an average of the gas composition reported by the CNG provider. In the time-averaged case shown here, a low-frequency ($\sim$0.05 Hz) 1% oscillation was observed in both mass-flow rates of the oxygen and CNG controllers, which was averaged-out because the data run usually lasted on the order of 1.5–2.5 min. However, for the comparisons made later, a 0.2 s data segment was used and the average water mole percent was computed for that particular time from the mass-flow controller data.

Figure 7a shows the experimental layout as implemented during the test campaign. Figure 7b shows a top view of the experimental setup as well as an absorption map for line a (7185.6 cm^{-1}) that has been overlaid on the experimental setup. Here, this corresponds to a

Table 3 Average run conditions: facility nozzle at $M = 2.2$

Run	Start time	Incoming-air temperature, K	Total temperature, K	Total pressure, psia	Water mole percent,[a] %	Reynolds number
AB	19:23:07	300	667	50	3.03	9.1×10^5
AC	19:36:21	300	1016	50	6.93	4.6×10^5
AF	21:26:20	589	667	50	1.11	9.1×10^5
AG	21:34:58	589	1016	50	4.94	4.6×10^5

[a]Assumes dry facility air.

horizontal cross section taken at midheight in the isolator. The first aspect that can be observed is that the most significant changes in the flow structure occur in the streamwise direction and consist of high and low regions of density, pressure, and temperature in the shock train. It is the goal here to detect these variations in good detail in the streamwise direction with an approximate spacing of the 14 LOS of 5 mm. Obviously, this is the reason for the indicated probing geometry of 14 beams being aligned nearly perpendicularly to the flow direction. Higher resolution will improve the quality of the data; however, as will be shown in part 2 of this paper, significant aspects of the shock structure can be measured even with the sparse sampling used in this experiment. The photodiode arrays as well as collimator arrays are mounted on standard 12 by 18 in. optical breadboards that are inserted into aluminum purge boxes. These purge boxes were sealed except for inlets and exit ports for N_2 purge gas and a face plate that had a rectangular hole slightly larger than the isolator windows. The isolator wall has the potential to reach 700–800 K during high-enthalpy runs; therefore, the front of each box was press-fitted against a ceramic firebrick cutout that insulated the purge box from the isolator wall. Finally, a mask insert restricting the photodiode field of view was found necessary for runs AC and AG, due to blackbody radiation associated with the interior walls of the isolator. The boxes were mounted on a much larger breadboard attached to the thrust stand rails, allowing the whole setup to move with the test rig as it thermally expanded. Compressed nitrogen was used to pressurize a LN_2 dewar for which the blowoff was used to cool and purge the boxes of ambient air. Excellent purge was achieved and no evidence of water vapor due to the regions outside the flow was observed during the experiments.

IV. Isolator Results and Discussion

This section details the accuracy and precision of the TDLAS measurements for the case of Mach 2 (no shock) isolator flow. The reason for focusing on the no-shock isolator flow is that it provides a baseline reference for the quality of data obtained in the subsequent experiments involving the shock train. These results can also be compared with similar experiments that have been performed in the past with single-line-of-sight measurements to illustrate improvements possible with the multiple lines of sight. This section starts this analysis by considering the temporal variations along one line-of-sight to assess the precision of a single measurement versus time. Next, it examines the spatial uniformity of the time-averaged measurements. Finally, the time- and space-averaged static pressure, temperature, and water molar fraction are compared with either pressure-tap data, CFD computations (static temperature), or the complete combustion model (water molar fraction). In all three cases, the comparisons are excellent, with the water molar fraction being the hardest to compare because of the uncertainty in the CNG composition. These results are then compared and contrasted to previous single-line-of-sight measurements.

The assessment of the measurement accuracy and precision are necessarily more difficult for the case of the Mach 2 (no-shock) isolator flow than for steady flow problems such as laminar flames, which have been studied extensively. Here, issues such as lacking high-quality data that can be used to compare the measurements with, flow unsteadiness, and small spatial variations in the flowfield will all impact the accuracy as well as precision of the measurements. In addition, systematic errors due to errors in the spectroscopic

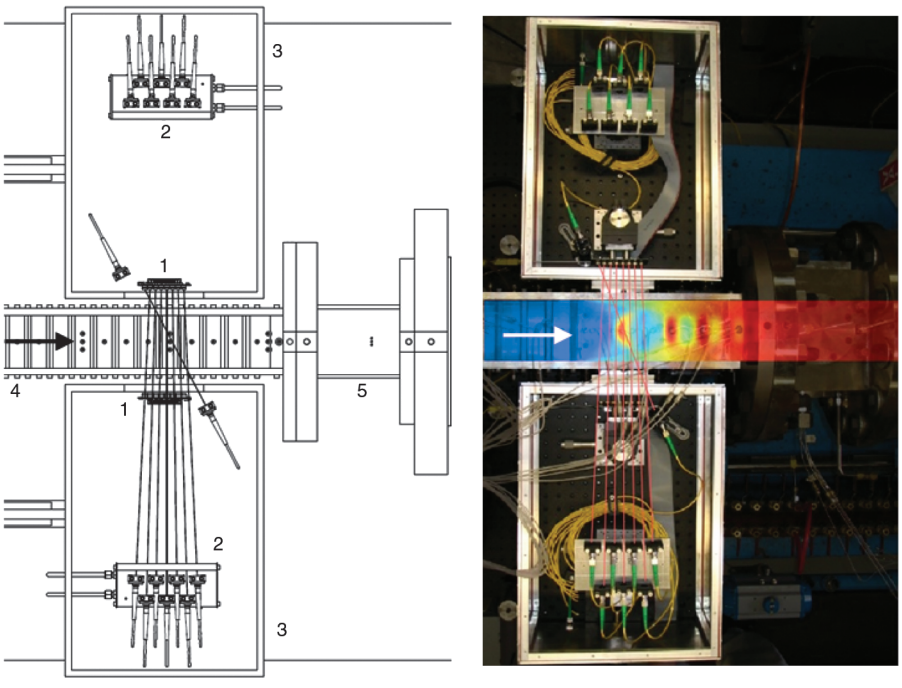

a) b)

Fig. 7 Experimental setup: a) schematic with labels for key components 1: photodiode arrays, 2: collimator arrays, 3: purge boxes, 4: isolator, and 5: extension piece (the arrow indicates the direction of the flow, and only eight beams going from the bottom purge box to the top one are shown, for clarity; another eight beams interlaced between those shown are also used) and b) photograph with an overlay depicting the shock-train structure in the isolator (the measurement plane occurs at midheight in the isolator).

parameters will affect the comparison. Nevertheless, excellent comparisons exist between static temperatures and calculations, static pressures and average wall pressure measurements, and water mole percent and complete combustion assumptions.

Figure 8 shows the measurements for a single LOS located 3.43 cm from the upstream edge of the window during run AB (no backpressure condition). At any given time, the data are of excellent quality and the temperature and water concentration can be deduced from the Boltzmann plot as well as pressure from the line width of line *a*. The fluctuations in static temperature and pressure are on the order of 3% and reflect variations in the rig operating conditions as well as the baseline estimation procedure used to process the data.

As can be seen in Fig. 9, excellent precision is obtained between identical flow conditions despite significant time difference between runs and the use of unheated or preheated air to the vitiator. Figure 9 also shows how the time-averaged spatially resolved data vary as a function of streamwise position in the duct. The maximum value of the amplitude variations is always less than 10% of the mean value (scale is $\pm 10\%$) and often much less. The data were acquired in this case by first averaging the spectra from the 200 different scans in one data segment. Multipeak Voigt fits were then used to fit each spectrum in the manner described in Sec. II to obtain the data in Fig. 9. The data segment was chosen by examining each run time during the course of each run when it was expected that no shock was present in the window. However, in case of run AG, the very front edge of a shock is beginning to enter the rear of the window, as confirmed by an inspection of the isolator pressure taps. All cases show that the LOS closest to the rear of the window exhibits a rise in pressure compared with the other LOS. This also appears to be the case for the pressure-tap data. It may be the case that a weak shock is attaching near the rear of the window, where there is a small break between the window and the TBC sidewall of the isolator. The error bars in Fig. 9 correspond to the standard statistical error bars from a curve fit. These error bars agree with the results reported in Fig. 8, because the error in the mean in that case roughly corresponds to the standard error bars in Fig. 9. Note that although standard errors are being reported, confidence intervals have not been provided. This requires knowledge of the underlying distribution of the data, which is difficult to determine and most likely not Gaussian. However, the small standard errors suggest that something other than statistical errors are causing the spatial oscillations such as local flow fluctuations. By averaging over these spatial oscillations, an increase in measurement precision is achieved.

Figure 10 shows that spatial oscillations also exist in the sidewall pressure measurements. As can be seen here, during run AC, the pressure fluctuates along the duct. The error bars indicate the calibration error of the pressure transducers; thus, the oscillations observed are due to flowfield variations. This should be expected for a turbulent flow. In an effort to eliminate these fluctuations, the three pressure taps that span the window region (one on the bottom side and two on the top side) are averaged together and compared with the spatially and temporally averaged TDLAS measurements. The comparison between the TDLAS measurements and pressure-tap measurements is presented in Table 4. As can be seen in the table, the agreement is excellent, with the worst disagreement being 3% for run AB and the average disagreement being 1.75% between TDLAS and the average pressure-tap pressure. This is less than the error bars for the TDLAS measurements, which have been taken to be $\pm 5\%$ (0.32 psia), due to possible systematic errors in the line-broadening parameters, in accordance with [34]. The errors for the pressure taps are the standard deviation of the mean of the three pressure taps located within the window region. Note that the TDLAS data show remarkable similarity between runs AB and AC and between runs AF and AG. The statistical precision of the TDLAS data can be determined from Fig. 9 to be approximately 0.04–0.07 psia, and so it would be much better than the pressure transducer data, which only exhibit a precision of 0.1–0.2 psia. At the current level of analysis, though, it will be difficult to determine the sources of these differences, because they could be due to a large number of factors involved in accurately determining the facility operating conditions.

Currently, the static temperature of the flow can only be compared with the CFD simulations. To perform this comparison properly, the path-integrated temperature must be determined from the CFD, as described in Secs. II.B and II.C. The comparison is shown in Table 5. As can be seen from this table, excellent agreement is found between the computed and the measured temperatures, with a maximum difference of 3.3% and an average difference of 2.3%. The error bars have been computed based on a $\pm 3\%$ systematic error plus the statistical error evident in Fig. 10.

Table 5 also shows the comparison between the facility-based computations and the TDLAS computations of water mole percent in the vitiated flow. The TDLAS results for the water mole percent are based on the TDLAS static pressures in Table 4, TDLAS static temperatures in Table 5, and TDLAS water concentrations. The ideal gas law is used to compute the total densities from the TDLAS static pressure and temperature, and the measurement errors are

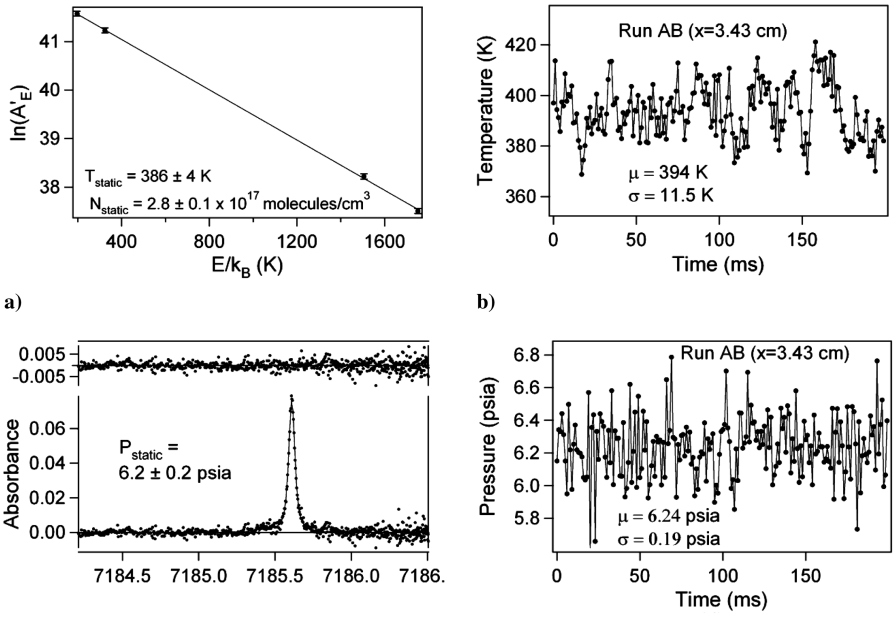

Fig. 8 Plots for the LOS at $x = 3.43$ cm from the upstream edge of the window: a) Boltzmann plot for one scan (0.3 ms), b) temporal variation of temperature versus time, c) spectrum for one scan, and d) pressure versus time.

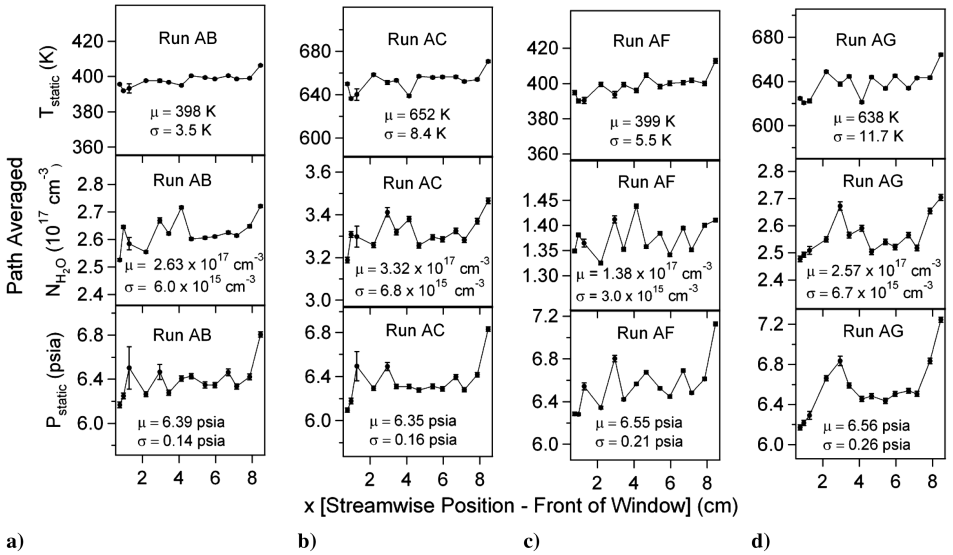

Fig. 9 Streamwise variation of time- and path-averaged static temperature, water concentration, and static pressure for run conditions a) AB, b) AC, c) AF, and d) AG. Scales are taken to be ±10% of the mean. The displayed error bars are fit error bars and do not reflect inaccuracies due to line parameters.

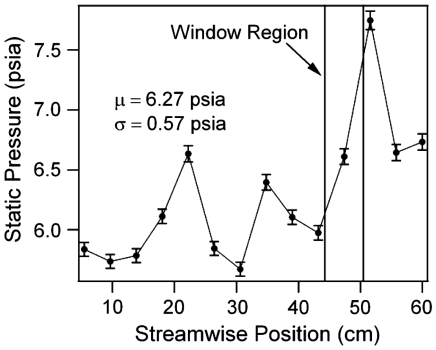

Fig. 10 Pressure measurements using conventional static pressure taps on the bottom side of the isolator as well as in the window region near the time the Mach 2 data was taken for run AC.

propagated through using standard methods. The facility computations are based on flow rates through facility-provided mass-flow controllers that provide the flow rate of air, compressed natural gas, and oxygen to the vitiator. The molar fraction of water is then computed based on complete combustion of the CNG mixture. Because the CNG is not pure, as detailed earlier, the maximum possible error of 8% has been used to determine the errors for the facility computations. In addition, the measured 0.28% water mole percent has been added in the computations for runs AF and AG to account for the water present in the facility air. The agreement between the TDLAS and the calculated water mole percent methods is quite good despite the approximations being made, with the facility agreeing with the TDLAS computations to the level of 7%, except for the case of run AF. There, the difference in these measurements is on the order of the facility air correction to the small amount of water produced under those conditions. In general, the agreement is within the error of the facility computations.

Before concluding this section, it is useful to compare the measurements with previous measurement campaigns in similar facilities. In particular, a straightforward comparison with the work of Upschulte et al. [6] is useful to see how the measurement accuracy and precision have increased. For that particular case, two LOS were used to probe the flow along an 18 cm path, which is almost a factor of 2 longer than the paths used in the current experiments (10.14 cm). In that work, the measured static temperatures were found to agree with the predicted static temperatures within 7–11%, which is a factor of 2–3 more than the maximum disagreements observed here. In addition, the water mole percent was observed to differ from the predicted water fractions by a factor of 17–56%, which is a factor of 1–3 more than the maximum disagreement observed in this work. However, as seen here, the lowest disagreements were observed with the highest water concentrations, suggesting that approximations used in computing the water fraction were also a factor in that work. Most of the improvement is probably due to the increase in the quality of the optical hardware over the course of the last eight years as well as more accurate determination of the absorption line parameters. Some of the differences could also be facility improvements. However, it is also the case that the use of multiple paths allows for averaging over spatial inhomogeneities that would be more difficult with two lines of sight. The work of Liu et al. [5] represents a more recent study (2005) of the test rig in research cell 22 and takes advantage of the improvements in optical hardware that

Table 4 Static pressure comparison

Run	TDLAS, psia	Pressure taps, psia	% difference (TDLAS-P. taps)
AB	6.39 ± 0.32	6.59 ± 0.20	−3.0%
AC	6.35 ± 0.32	6.49 ± 0.09	−2.2%
AF	6.55 ± 0.33	6.65 ± 0.08	−1.5%
AG	6.56 ± 0.33	6.58 ± 0.14	−0.3%

Table 5 Path-averaged static temperature comparison and water mole percent

	Temperature			Water mole percent		
Run	TDLAS, K	CFD. K	% difference (TDLAS-CFD)	TDLAS, %	Facility computation, %	% difference (TDLAS facility)
AB	398 ± 4	389	2.2%	3.30 ± 0.20	3.07 ± 0.25	7.32
AC	652 ± 10	630	3.3%	6.83 ± 0.38	7.09 ± 0.57	−3.7
AF	399 ± 4	389	2.6%	1.68 ± 0.10	1.44 ± 0.28	17
AG	638 ± 11	630	1.25%	5.04 ± 0.29	5.27 ± 0.50	−4.4

have been recently made. It shows many of the improvements in data quality that can be observed by comparing the current study with that by Upschulte et al. [6]. Unfortunately, no comparisons with the predicted facility vitiation conditions were made, and so a straightforward comparison cannot be made. However, it appears that the measurement quality is more in agreement with the results given here. The extent of LOS multiplexing (14 LOS) and data acquisition applied in this study is new.

V. Conclusions

The design, setup, and measurement accuracy and precision of a 16-LOS tunable diode laser absorption system has been demonstrated. The first-ever measurements of static pressure using line-width broadening in a scramjet isolator have also been reported. The accuracy of the measurements is excellent, with average differences on the order of 2% for static pressure when compared with the pressure taps, and the temperature agreement with CFD is on the order of 2%. The comparison of water mole percent is more complex and requires that approximations be made in facility computations. Nevertheless, excellent agreement is once again seen, with the exception of run AF ($\chi \sim 1.5\%$), where the disagreement is 17% but is still within the facility error bars. The time resolution of the sensor is 1 μs for short time periods ($\sim$1 s), which enables the measurement of phenomena that repeat, such as the shock train in part 2 of this paper. However, for single-event transients, it is necessary to improve the data acquisition so that data can be collected continuously for much longer periods. The hardware and software developed for this study pave the way for measurements of shock structures in the isolator that are presented in part 2 of this paper. Furthermore, the system described here is scalable and should enable high-precision spatial and spectrally multiplexed TDLAS measurements for supersonic flow characterization, combustion product analysis, and real-time monitoring of the flow environment. At present, 16 beam paths are employed, but the system could be readily extended to 128 beam paths with the appropriate optical access. The importance of this advancement is more evident in the following paper, which focuses on the analysis of transient behavior.

Acknowledgments

This work was supported by the U.S. Air Force Office of Scientific Research (Michael Berman, Program Manager) and the National Research Council, which sponsored C. D. Lindstrom as a postdoctoral fellow. The authors thank the RC18 test team (Matt Streby, Steven Lin, Steve Ennekin, and Paul Kennedy) for rig operation and test setup.

References

[1] Baer, D. S., Paul, J. B., Gupta, M., and O'Keefe, A., "Sensitive Absorption Measurements in the Near-Infrared Region Using Off-Axis Integrated-Cavity-Output Spectroscopy," *Applied Physics B (Lasers and Optics)*, Vol. 75, No. 2–3, 2002, pp. 261–265. doi:10.1007/s00340-002-0971-z

[2] Druy, M., Frish, M., and Kessler, W., "Molecular Spectroscopy Workbench from Laboratory Technique to Process Gas Sensor: Maturation of Tunable Diode Laser Absorption Spectroscopy," *Spectroscopy*, Vol. 21, No. 3, 2006, pp. 14–18.

[3] Silver, J. A., and Wood, W. R., "Miniature Gas Sensor for Monitoring Biological Space Environments," *Diode Lasers and Applications in Atmospheric Sensing*, Proceedings of SPIE, Vol. 4817, SPIE–The International Society for Optical Engineering, 2002, pp. 73–81. doi:10.1117/12.452092

[4] Williams, S., Barone, D., Barhorst, T., Jackson, K., Lin, K.-C., Masterson, P., Zhao, Q., and Sappey, A., "Diode Laser Diagnostics of High Speed Flows," AIAA Paper 2006-7999, Nov. 2006.

[5] Liu, J. T. C., Rieker, G. B., Jeffries, J. B., Gruber, M. R., Carter, C. D., Mathur, T., and Hanson, R. K., "Near-Infrared Diode Laser Absorption Diagnostic for Temperature and Water Vapor in a Scramjet Combustor," *Applied Optics*, Vol. 44, No. 31, 2005, pp. 6701–6711. doi:10.1364/AO.44.006701

[6] Upschulte, B. L., Miller, M. F., and Allen, M. G., "Diode Laser Sensor for Gasdynamic Measurements in a Model Scramjet Combustor," *AIAA Journal*, Vol. 38, No. 7, 2000, pp. 1246–1252. doi:10.2514/2.1094

[7] Lyle, K. H., Jeffries, J. B., and Hanson, R. K., "Diode-Laser Sensor for Air-Mass Flux 1: Design and Wind-Tunnel Validation," *AIAA Journal*, Vol. 45, No. 9, 2007, pp. 2204–2212. doi:10.2514/1.26360

[8] Lyle, K. H., Jeffries, J. B., Hanson, R. K., and Winter, M., "Diode-Laser Sensor for Air-Mass Flux 2: Nonuniform Flow Modeling and Aeroengine Tests," *AIAA Journal*, Vol. 45, No. 9, 2007, pp. 2213–2223. doi:10.2514/1.27683

[9] Miller, M. F., Kessler, W. J., and Allen, M. G., "Diode Laser-Based Air Mass Flux Sensor for Subsonic Aeropropulsion Inlets," *Applied Optics*, Vol. 35, No. 24, 1996, pp. 4905–4912. doi:10.1364/AO.35.004905

[10] Matsuo, K., Miyazato, Y., and Kim, H.-D., "Shock Train and Psuedo-Shock Phenomena in Internal Gas Flows," *Progress in Aerospace Sciences*, Vol. 35, No. 1, 1999, pp. 33–100. doi:10.1016/S0376-0421(98)00011-6

[11] Carroll, B. F., and Dutton, J. C., "Characteristics of Multiple Shock Wave/Turbulent Boundary-Layer Interactions in Rectangular Ducts," *Journal of Propulsion and Power*, Vol. 6, No. 2, 1990, pp. 186–193. doi:10.2514/3.23243

[12] Carroll, B. F., and Dutton, J. C., "Multiple Normal Shock Wave/Turbulent Boundary-Layer Interactions," *Journal of Propulsion and Power*, Vol. 8, No. 2, 1992, pp. 441–448. doi:10.2514/3.23497

[13] Om, D., and Childs, M. E., "Multiple Transonic Shock-Wave/Turbulent Boundary-Layer Interaction in a Circular Duct," *AIAA Journal*, Vol. 23, No. 10, 1985, pp. 1506–1511. doi:10.2514/3.9117

[14] Liu, X., Jeffries, J. B., and Hanson, R. K., "Measurement of Nonuniform Temperature Distributions Using Line-of-Sight Spectroscopy," *AIAA Journal*, Vol. 45, No. 2, 2007, pp. 411–419. doi:10.2514/1.26708

[15] Wondraczek, L., Khorsandi, A., Willer, U., heide, G., Schade, W., and Frischat, G. H., "Mid-Infrared Laser-Tomographic Imaging of Carbon Monoxide in Laminar Flames By Difference Frequency Generation," *Combustion and Flame*, Vol. 138, No. 1–2, 2004, pp. 30–39. doi:10.1016/j.combustflame.2004.03.011

[16] Anderson, P. W., "Pressure Broadening in the Microwave and Infrared Regions," *Physical Review*, Vol. 76, 1949, pp. 647–661. doi:10.1103/PhysRev.76.647

[17] Delaye, C., Hartmann, J.-M., and Taine, J., "Calculated Tabulations of H_2O Line Broadening by H_2O, N_2, O_2, and CO_2 at High Temperature," *Applied Optics*, Vol. 28, No. 23, 1989, pp. 5080–5087. doi:10.1364/AO.28.005080

[18] Durry, G., Zeninari, V., Parvitte, B., barbu, T. L., Lefevre, F., Ovarlez, J., and Gamache, R. R., "Pressure-Broadening Coefficients and Line Strengths of H_2O Near 1.39 um: Application to the in Situ Sensing of the Middle Atmosphere with Balloonborne Diode LASERS," *Journal of Quantitative Spectroscopy and Radiative Transfer*, Vol. 94, No. 3–4, 2005, pp. 387–403. doi:10.1016/j.jqsrt.2004.09.033

[19] Liu, X., Zhou, X., Jeffries, J. B., and Hanson, R. K., "Experimental Study of H_2O Spectroscopic Parameters in the Near-IR (6940–7440 cm^{-1}) for Gas Sensing Applications at Elevated Temperature," *Journal of Quantitative Spectroscopy and Radiative Transfer*, Vol. 103, No. 3, 2007, pp. 565–577. doi:10.1016/j.jqsrt.2006.07.008

[20] Rothman, L. S., Jacquemart, D., Barbeb, A., Benner, C. D., Birkd, M., Browne, L. R., et al., "The HITRAN 2004 Molecular Spectroscopic Database," *Journal of Quantitative Spectroscopy and Radiative Transfer*, Vol. 96, No. 2, 2005, pp. 139–204. doi:10.1016/j.jqsrt.2004.10.008

[21] Bernath, P. F., "Rotational Spectroscopy," *Spectra of Atoms and Molecules*, 2nd ed., Oxford Univ. Press, New York, 2005, pp. 166–280.

[22] Herzberg, G., "Rotation and Vibration of Diatomic Molecules; Interpretation of Infrared and Raman Spectra," *Molecular Spectra and Molecular Structure. 1: Spectra of Diatomic Molecules*, 2nd ed., Krieger, Malabar, FL, 1950, pp. 66–141.

[23] Mukamel, S., "Semiclassical Simulation of the Optical Response Functions," *Nonlinear Optical Spectroscopy*, Oxford Univ. Press, New York, 1995, pp. 187–206.

[24] Rothman, L. S. et al., "The HITRAN Molecular Spectroscopic Database and HAWKS (HITRAN Atmospheric Workstation): 1996 Edition," *Journal of Quantitative Spectroscopy and Radiative Transfer*, Vol. 60, No. 5, 1998, pp. 665–710. doi:10.1016/S0022-4073(98)00078-8

[25] Humlíček, J., "Optimized Computation of the Voigt and Complex Probability Functions," *Journal of Quantitative Spectroscopy and Radiative Transfer*, Vol. 27, No. 4, 1982, pp. 437–444. doi:10.1016/0022-4073(82)90078-4

[26] Ouyang, X., and Varghese, P. L., "Line-of-Sight Absorption Measurements of High Temperature Gases with Thermal and Concentration Boundary Layers," *Applied Optics*, Vol. 28, No. 18, 1989, pp. 3979–3984. doi:10.1364/AO.28.003979

[27] Chung, K. B., Gouldin, F. C., and Wolga, G. J., "Experimental Reconstruction of the Spatial Density Distribution of a Nonreacting Flow with a Small Number of Absorption Measurements," *Applied Optics*, Vol. 34, No. 24, 1995, pp. 5492–5500. doi:10.1364/AO.34.005492

[28] Lindstrom, C., Tam, C.-J., Davis, D., Eklund, D., and Williams, S., "Diode Laser Absorption Tomography of 2-D Supersonic Flow," AIAA Paper 2007-5014, July 2007.

[29] Torniainen, E. D., and Gouldin, F. C., "Tomographic Reconstruction of 2-D Absorption Coefficient Distributions from a Limited Set of Infrared Absorption Data," *Combustion Science and Technology*, Vol. 131, Nos. 1–6, 1998, pp. 85–105. doi:10.1080/00102209808935756

[30] Torniainen, E. D., Hinz, A. K., and Gouldin, F. C., "Tomographic Analysis of Unsteady, Reacting Flows: Numerical Investigation," *AIAA Journal*, Vol. 36, No. 7, 1998, pp. 1270–1278. doi:10.2514/2.509

[31] Lepere, M., Henry, A., Valentin, A., and Camy-Peyret, C., "Diode-Laser Spectroscopy: Line Profiles of H_2O in the Region of 1.39 um," *Journal of Molecular Spectroscopy*, Vol. 208, No. 1, 2001, pp. 25–31. doi:10.1006/jmsp.2001.8372

[32] Toth, R. A., "Extensive Measurements of H_2O Line Frequencies and Strengths: 5750 to 7965 cm^{-1}," *Applied Optics*, Vol. 33, No. 21, 1994, pp. 4851–4867. doi:10.1364/AO.33.004851

[33] Nagali, V., Chou, S. I., Baer, D. S., and Hanson, R. K., "Diode-Laser Measurements of Temperature-Dependent Half-Widths of H_2O Transitions in the 1.4 um Region," *Journal of Quantitative Spectroscopy and Radiative Transfer*, Vol. 57, No. 6, 1997, pp. 795–809. doi:10.1016/S0022-4073(97)00011-3

[34] Gamache, R. R., Hartmann, J.-M., and Rosenmann, L., "Collisional Broadening of Water Vapor Lines. 1: A Survey of Experimental Results," *Journal of Quantitative Spectroscopy and Radiative Transfer*, Vol. 52, No. 3/4, 1994, pp. 481–499. doi:10.1016/0022-4073(94)90175-9

[35] Gruber, M., Donbar, J., Jackson, K., Mathur, T., Baurle, R., Eklund, D., and Smith, C., "Newly Developed Direct-Connect High-Enthalpy Supersonic Combustion Research Facility," *Journal of Propulsion and Power*, Vol. 17, No. 6, 2001, pp. 1296–1304. doi:10.2514/2.5878

[36] Mathur, T., Gruber, M., Jackson, K., Donbar, J., Donaldson, W., Jackson, T., and Billig, F., "Supersonic Combustion Experiments with a Cavity-Based Fuel Injector," *Journal of Propulsion and Power*, Vol. 17, No. 6, 2001, pp. 1305–1312. doi:10.2514/2.5879

R. Lucht
Associate Editor